RESEARCH ARTICLE

National Science Open
3: 20230085, 2024
https://doi.org/10.1360/nso/20230085

Information Sciences

Special Topic: Microwave Vision and SAR 3D Imaging

RM-CSTV: An effective high-resolution method of non-line-of-sight millimeter-wave radar 3-D imaging

Xinyuan Liu, Shunjun Wei*, Wei Pu, Xiang Cai, Yanbo Wen, Shisheng Guo, Lingjiang Kong & Xiaoling Zhang

School of Information and Communication Engineering, University of Electronic Science and Technology of China, Chengdu 611731, China

*Corresponding author (email: weishunjun@uestc.edu.cn)

Received 15 December 2023; Revised 26 January 2024; Accepted 28 May 2024; Published online 20 August 2024

Abstract: Non-line-of-sight (NLOS) imaging is a novel radar sensing technology that enables the reconstruction of hidden targets. However, it may suffer from synthetic aperture length reduction caused by ambient occlusion. In this study, a complex total variation (CTV) regularization-based sparse reconstruction method for NLOS three-dimensional (3-D) imaging by millimeter-wave (mmW) radar, named RM-CSTV method, is proposed to improve imaging quality and speed. In this scheme, the NLOS imaging model is first introduced, and associated geometric constraints for NLOS objects are established. Second, an effective high-resolution NLOS imaging method based on the range migration (RM) kernel and complex sparse joint total variation constraint, dubbed as modified RM-CSTV, is proposed for 3-D high-resolution imaging with edge information. The experiments with multi-type NLOS targets show that the proposed RM-CSTV method can provide effective and high-resolution NLOS targets 3-D imaging.

Keywords: NLOS imaging, 3-D-SAR, 3-D imaging, sparse reconstruction

INTRODUCTION

Non-line-of-sight (NLOS) imaging is a novel method used to reconstruct hidden targets located behind corners. The NLOS imaging technique leverages the characteristics of multipath electromagnetic (EM) propagation. As EM and light waves bounce off the surface of the line-of-sight (LOS) medium, they illuminate the hidden target and reflect back to the detector. Through the process, valuable information such as the range, azimuth, and geometry of the NLOS target can be detected from the multipath echo. With the capacity of all-day and all-weather working, the NLOS radar imaging has received widespread attention. Combined with the three-dimensional (3-D) synthetic aperture radar (SAR) imaging algorithm, it becomes possible to reconstruct and identify high-precision stereo images of hidden targets located behind obstacles.

The NLOS imaging technology originated from the study of optical methods. In recent years, there have been many studies on NLOS scene imaging in the optical field [1–5]. In ref. [6], based on the time-of-flight (TOF) theory, the scholars utilize a femtosecond laser and an ultrafast photodetector array to reconstruct the 3-D images of the hidden objects. In ref. [7], Rapp *et al*. exploited an arc scanning light source to control the illuminated portion of the hidden area and achieved 2.5 dimensional veiled scene reconstruction. For the extraction of hidden target details, Liu *et al*. [8] proposed an NLOS imaging algorithm based on a Bayesian framework to achieve the recovery of fine details. However, the optical NLOS sensing requires expensive optical equipment and is heavily affected by meteorology. Other NLOS imaging technologies, such as acoustic [9] and WiFi [10, 11], also have similar limitations. Compared to optical devices, radar is inexpensive and stable. Meanwhile, there are several 3-D imaging achievements in the radar field. Hence, NLOS radar imaging has great potential.

T-shaped hidden scene is a research hotspot of existing radar NLOS sensing. The target and the radar are blocked by the obstacle, and the EM waves cannot illuminate the target in the LOS direction [12–19]. In ref. [20], Li *et al*. achieved multi-hidden target localization by measuring and eliminating the ghosts caused by multipath. For LOS 3-D radar imaging [21–27], Wang et al. [28] proposed a perceptual learning framework by unfolding the fast iterative shrinkage-thresholding algorithm (FISTA) and exploring the sparse prior. For LOS 3-D microwave vision [29–31], several SAR 3-D imaging systems and methods are discussed. In refs. [32, 33], the scholars focus on tomographic synthetic aperture radar (TomoSAR) and proposed a method dubbed ATASI-Net, which overcomes the drawbacks of the traditional algorithm, such as weak noise resistance and high computational complexity.

For radar NLOS sensing, the main research direction is to focus on 3-D positioning [19, 20, 34–36]. In order to realize NLOS 3-D imaging, we have carried out a series of studies [37–41]. We proposed the MSBP algorithm for the looking around corner (LAC) case and verified the method by the experiment data collected by MIMO millimeter wave array antennas [42]. Although high-resolution 3-D reconstruction of hidden targets was achieved, the signal undersampling problem caused by complex NLOS scenes exists, which leads to the failure of proposed algorithm. Thus, a no prior information required joint compressed sensing algorithm with total variation (TV) regularization, L_1 norm and range migration (RM) kernel called RM-CSTV is proposed to achieve 3-D high-resolution imaging.

In this study, for the echo model of NLOS imaging is different from that of LOS region due to the multipath effect in electromagnetic propagation, the matrix model and wave-number domain model of NLOS echo are first analyzed theoretically, and the detection and correction methods without prior information without prior information of NLOS targets are given according to NLOS geometric constraints. Additionally, aiming at the sparse characteristics of NLOS echoes, we propose a 3-D sparse reconstruction method of NLOS based on L_1 norm and complex TV regular, and an effective 3-D imaging method based on RM kernel function is proposed to solve the problem of huge computation. Furthermore, we build up NLOS 3-D imaging experimental system to verify the effectiveness of the proposed method. Finally, we summarize the content of this study.

The main contribution of this article are as follow: (1) a geometric constraint based NLOS target detecting method for array SAR 3-D imaging is proposed, which provides a theoretical basis for 3-D NLOS target detection; (2) compared with present algorithm and our previous [42], CSTV method avoids the loss of contour information, and exploits the sparse characteristic of NLOS echo to achieve high resolution imaging; (3) by introducing the RM kernel, the calculation time of RM-CSTV method reduced two orders of magnitude compared with CSTV method, which provides a possibility for practical application of NLOS 3-D imaging. The rest of this study is organized as follows. Section 2 introduces the problem formulation related to NLOS 3-D imaging is analyzed. In section 3, the theories and algorithms flows of NLOS targets 3-D effective reconstruction is proposed. The experimental scene and 3-D imaging results are shown and discussed in

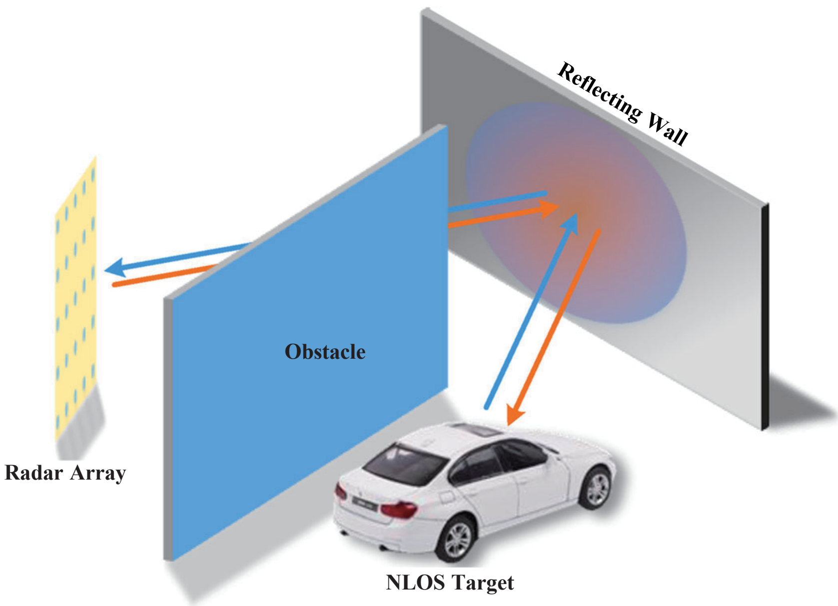

Figure 1 The layout of a typical LAC scene. The wall is used as an intermediary mmW propagating, and the echoes are received from the three-bounces path.

section 4. Finally, we give a conclusion in section 5.

PROBLEM FORMULATION

In this section, we present the basic theory for mmW NLOS 3-D imaging in the "T" type LAC scene. First, the geometric constraints of LAC scene is discussed for detecting the reflecting walls. Then, to obtain high-resolution imaging, the CS theory based model of NLOS radar echo is proposed. Finally, the theoretical resolution for mmW NLOS imaging system is analyzed.

A typical NLOS scene is shown in Figure 1. The millimeter wave undergoes reflection by the reflecting surface to illuminate the NLOS target, and is subsequently received by the array after undergoing three scatterings. The Considering distance of representation in linear array scanning mmW radar NLOS 3-D imaging, the single trip of signal R can be described as

$$R = R_{\text{los}} + R_{\text{nlos}}. \tag{1}$$

Specifically, the scattering process can be seen as ideally-reflection when the reflecting surface roughness height Δh satisfied

$$\Delta h \leqslant \frac{\lambda}{8\cos\theta_{\text{in}}}, \tag{2}$$

where λ is signal wave length, θ_{in} is the angle of incidence. In this scenario, deterministic reflection path exhibit, the transmitting and reflecting distances of given array element for the designated target are equivalent.

Through the three-bounce path, the single point NLOS target echo can be described as

$$\begin{aligned} s(t,\tau_{\text{nlos}}) = {} & \sigma * \rho_r(\theta_i,\theta_o) \\ & * \exp\left\{ \mathrm{j}2\pi f_0 (t-\tau_{\text{nlos}}) + \mathrm{j}\pi K (t-\tau_{\text{nlos}})^2 \right\}, \end{aligned} \tag{3}$$

where $\tau_{\mathrm{nlos}} = 2\left(R_{\mathrm{los}} + R_{\mathrm{nlos}}\right)/c$, f_0 denotes carrier frequency, σ is the scattering coefficient of target, $\rho_r\left(\theta_i, \theta_o\right)$ denotes bidirectional reflection distribution function (BRDF), influenced by angle of incidence θ_i and angle of emergence θ_o. K is frequency slope.

Expanding to 3-D targets imaging, the echo can be described by exploiting the CS method:

$$\mathbf{S} = \mathbf{\Psi}\mathbf{x}' + \mathbf{n}, \tag{4}$$

where $\mathbf{S} \in \mathbb{C}^{M\times 1}$ is signal echo vector, $\mathbf{\Psi} \in \mathbb{C}^{M\times N_x N_y}$ is the measure matrix. $\mathbf{x}' \in \mathbb{C}^{N_x N_y \times 1}$ is the scattering coefficient of virtual NLOS targets, $\mathbf{n}$ is the noise.

Additionally, expressing eq. (3) in wavenumber domain for reducing the computational complexity, we can obtain the scattering coefficient $x\left(\mathbf{P}_s, r\right)$ of range plane r as follows:

$$x\left(\mathbf{P}_s, r\right) = \int IFT_{2D}\left(FT_{2D}\left(S\left(\mathbf{P}_a, k\right)\right) \times k_y \exp\left\{\mathrm{j}k_y r\right\}\right)\mathrm{d}k, \tag{5}$$

where $IFT_{2D}\left(\cdot\right)$ is the two-dimensional inverse Fourier transform operator, $\mathbf{P}_s$ is the position of scattering coefficient, $\mathbf{P}_a$ is the antenna phase center, $k = \left(2\pi\left(f + f_0\right)\right)/c$, and k_y can be denoted as

$$k_y = \sqrt{4k^2 - {k_x}^2 - {k_z}^2}, {k_x}^2 + {k_z}^2 \leqslant 4k^2. \tag{6}$$

In this study, we exploit geometrical relationships in the NLOS scene to reconstruct the hidden target in a real position. As shown in eq. (4), the NLOS targets are reconstructed in a virtual position with normal LOS objects.

Assuming that the reflective surface is similar to vertical and flat, which can be seen as the mirror reflector for mmW radar wave. Based on the 2D image, the position of the reflective wall can be determined. Considering the x-y axis in $z = z_0$ slice, the reflective surface is described as $Ax + By + C = 0$.

Hence, the relationship between position of virtual target $\mathbf{P}_T'$ and real target $\mathbf{P}_T$ is satisfied:

$$\begin{aligned}\mathbf{P}_T &= \begin{bmatrix} \frac{B^2-A^2}{A^2+B^2} & \frac{-2AB}{A^2+B^2} & 0 \\ \frac{-2AB}{A^2+B^2} & \frac{A^2-B^2}{A^2+B^2} & 0 \\ 0 & 0 & 1 \end{bmatrix} \mathbf{P}_{T'} - \begin{bmatrix} \frac{2BC}{A^2+B^2} \\ \frac{2AC}{A^2+B^2} \\ 0 \end{bmatrix} \\ &= \mathbf{M}_S \mathbf{P}_T{}' - \mathbf{E}. \end{aligned} \tag{7}$$

The equal-height slice of NLOS scene is shown in Figure 2. The target $\mathbf{T}$ is located at $\mathbf{P}_T = \left(x_0, y_0, z_0\right)$, and the reflecting wall $\mathbf{W}_1$ is the intermediary for multi-path echo. The radar antenna array $\mathbf{A}$ is located between the points $\mathbf{A}_1$ and $\mathbf{A}_2$. As shown in Figure 2, for the impact of $\mathbf{W}_2$, which might be buildings or cars in the urban environment, the direct path between antenna and target is blocked. The imaging space that can provide a direct echo for radar is called LOS region Ω_{los}. And the hidden space caused by obstacles is called NLOS region Ω_{nlos}. The mainly propagation of NLOS echo is constituted by three parts of bounces: $\mathbf{A} \rightarrow \mathbf{W}_1 \rightarrow \mathbf{T} \rightarrow \mathbf{W}_1 \rightarrow \mathbf{A}$ [42], where $\mathbf{A}$ is on the line segment $\overline{\mathbf{A}_1\mathbf{A}_2}$.

For the relationship shown in Figure 2, the virtual NLOS targets can be detected by the following constraints:

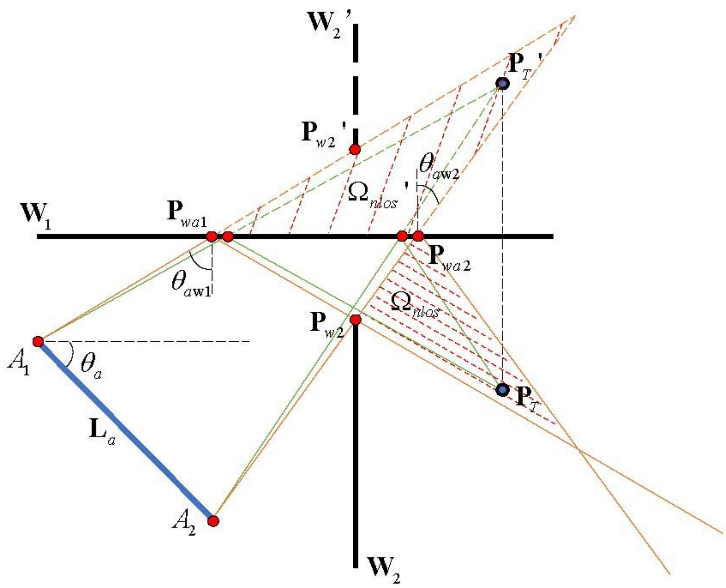

Figure 2 The Geometric relationship between radar array, reflecting wall and NLOS target.

$$\begin{cases} \mathbf{n}_w \cdot (\mathbf{P}_T{}' - \mathbf{W}_{11}) \geqslant 0, \\ ||\mathbf{P}_{WT1} - \mathbf{P}_{wa1}|| \leqslant ||\mathbf{P}_{wa1} - \mathbf{P}_{wa2}||, \\ ||\mathbf{P}_{WT1} - \mathbf{P}_{wa2}|| \leqslant ||\mathbf{P}_{wa1} - \mathbf{P}_{wa2}||, \\ ||\mathbf{P}_{WT2} - \mathbf{P}_{wa1}|| \leqslant ||\mathbf{P}_{wa1} - \mathbf{P}_{wa2}||, \\ ||\mathbf{P}_{WT2} - \mathbf{P}_{wa2}|| \leqslant ||\mathbf{P}_{wa1} - \mathbf{P}_{wa2}||, \end{cases} \tag{8}$$

where $\mathbf{A}_1$ and $\mathbf{A}_2$ are the two endpoint coordinate vectors of the antenna array, and $\mathbf{W}_{11}$ is the point on the reflecting wall $\mathbf{W_1}$. The incident point of the echo corresponding to the end of the radar array on the reflecting wall are $\mathbf{P}_{WT1}$ and $\mathbf{P}_{WT2}$, which can be calculated by

$$\mathbf{P}_{WT1} = \mathbf{A}_1 + \frac{(\mathbf{W}_{11} - \mathbf{A}_1) \times \mathbf{W}_1}{(\mathbf{P}_T{}' - \mathbf{A}_1) \times \mathbf{W}_1} (\mathbf{P}_T{}' - \mathbf{A}_1), \tag{9}$$

$$\mathbf{P}_{WT2} = \mathbf{A}_2 + \frac{(\mathbf{W}_{11} - \mathbf{A}_2) \times \mathbf{W}_1}{(\mathbf{P}_T{}' - \mathbf{A}_2) \times \mathbf{W}_1} (\mathbf{P}_T{}' - \mathbf{A}_2). \tag{10}$$

METHODOLOGY

In this section, the CS theory based NLOS 3-D imaging method is proposed. The 3-D reconstruction is divided into three steps: high-resolution imaging, reflecting surface judgment, and virtual targets adjusting. Meanwhile, the CS algorithms working in time-domain with high dimension matrix-ector operators employed in the optimization iterations generate large-scale storage of the measurement matrix and huge computational complexity. We proposed a novel RMA kernel-based STV 3-D imaging method to overcome these shortcoming. In this section, the sparse and total variation regularization operator combined (STV) high-resolution 3-D targets reconstructing method is introduced firstly. And then by exploiting the geometric constraints, we correct the virtual target to real position without any previous knowledge. At last, the RMA kernel is embedded into STV to improve the calculation speed.

The sparse-TV algorithm

Considering the CS theory, the echo in eq. (11) can be transfered into the following function:

$$\mathbf{S}_{\mathrm{NLOS}} = \mathbf{\Psi}\mathbf{x}_v + \mathbf{n}, \tag{11}$$

where $\mathbf{S}_{\mathrm{NLOS}} \in \mathbb{C}^{MN\times 1}$ is NLOS echo vector, $\mathbf{\Psi} \in \mathbb{C}^{MN\times N_x N_z}$ is the measure matrix proposed in ref. [43]. $\mathbf{x}_v \in \mathbb{C}^{N_x N_z \times 1}$ is the scattering coefficient of virtual NLOS targets, $\mathbf{n}$ is the noise.

Generally, to obtain high-resolution imaging, eq. (11) is solved by the following optimization method:

$$\begin{gathered} \min \alpha_1 \|\mathrm{CTV}(\mathbf{x})\|_1 + \alpha_2 \|\mathbf{x}\|_1, \\ \text{s.t.} \ \|\mathbf{S} - \mathbf{\Psi}\mathbf{x}\|_2^2, \end{gathered} \tag{12}$$

where $\|\mathbf{x}\|_1$ is used to characterize sparsity, $\|\cdot\|_{TV}$ denotes the 2D TV norm, which is using for preserving the contour information. α_1 and α_2 are the parameters for balancing the influence of these regular terms. Considering that the NLOS targets are isotropy, CTV operator can be described as

$$\mathrm{CTV}(\mathbf{x}) = \left(\mathrm{Re}(\nabla_x), \mathrm{Im}(\nabla_x), \mathrm{Re}\left(\nabla_y\right), \mathrm{Im}\left(\nabla_y\right)\right), \tag{13}$$

with

$$\begin{aligned} &\mathrm{Re}\{\nabla_x\}_{m,n} = \mathrm{Re}\{x\}_{m,n} - \mathrm{Re}\{x\}_{m+1,n}, \mathrm{Re}\{\nabla_x\}_{N,n} = 0, \\ &\mathrm{Re}\left\{\nabla_y\right\}_{m,n} = \mathrm{Re}\{x\}_{m,n} - \mathrm{Re}\{x\}_{m,n+1}, \mathrm{Re}\{\nabla_x\}_{m,N} = 0, \\ &\mathrm{Im}\{\nabla_x\}_{m,n} = \mathrm{Im}\{x\}_{m,n} - \mathrm{Im}\{x\}_{m+1,n}, \mathrm{Im}\{\nabla_x\}_{N,n} = 0, \\ &\mathrm{Im}\left\{\nabla_y\right\}_{m,n} = \mathrm{Im}\{x\}_{m,n} - \mathrm{Im}\{x\}_{m,n+1}, \mathrm{Im}\left\{\nabla_y\right\}_{m,N} = 0, \end{aligned} \tag{14}$$

where $\mathbf{I} \in \mathbb{R}^{\mathbf{N_x}\times\mathbf{N_x}}$ is the unit matrix.

Hence, the estimation of scattering coefficient $\hat{\mathbf{x}}$ can be transformed into the following unconstrained optimization problem:

$$\hat{\mathbf{x}} = \min_{\mathbf{x}} \alpha_1 \|\mathrm{CTV}(\mathbf{x})\|_1 + \alpha_2 \|\mathbf{x}\|_1 + \frac{1}{2}\|\mathbf{S} - \mathbf{\Psi}\mathbf{x}\|_2^2. \tag{15}$$

Convert eq. (15) to the following two variable representations:

$$\begin{gathered} \min \tfrac{1}{2}\|\mathbf{\Psi}\mathbf{x} - \mathbf{S}\|_2^2 + \alpha_1 \|\mathbf{z}_1\|_1 + \alpha_2 \|\mathbf{z}_2\|_1, \\ \text{s.t.} \ \mathbf{z}_1 = \mathrm{CTV}(\mathbf{x}), \mathbf{z}_2 = \mathbf{x}. \end{gathered} \tag{16}$$

By introducing Lagrangian multiplier $\mathbf{u} = \left[\mathbf{u}_1^{\mathrm{T}}, \mathbf{u}_2^{\mathrm{T}}\right]^{\mathrm{T}}$, the argument Lagrangian function can be described as

$$\begin{aligned} L(\mathbf{x}, \mathbf{z}, \mathbf{u}) = {} & \frac{1}{2}\|\mathbf{\Psi}\mathbf{x} - \mathbf{S}\|_2^2 + \alpha_1 \|\mathbf{z}_1\|_1 + \alpha_2 \|\mathbf{z}_2\|_1 \\ & + \mathbf{u}_1{}^{\mathrm{T}}(\mathrm{CTV}(\mathbf{x}) - \mathbf{z}_1) + \mathbf{u}_2{}^{\mathrm{T}}(\mathbf{x} - \mathbf{z}_2) \\ & + \frac{\lambda}{2}\|\mathrm{CTV}(\mathbf{x}) - \mathbf{z}_1\|_2^2 + \frac{\lambda}{2}\|\mathbf{x} - \mathbf{z}_2\|_2^2. \end{aligned} \tag{17}$$

Hence, the scattering coefficient **x** in eq. (17) can be solved by the following three steps [44].

Step 1: Minimized the scattering coefficient **x**:

$$\mathbf{x}^{k+1} = \min_{\mathbf{x}} \frac{1}{2} \|\mathbf{\Psi x} - \mathbf{S}\|_2^2 + \frac{\lambda}{2} \left\|\mathrm{CTV}\left(\mathbf{x}^{\mathrm{k}}\right) - \mathbf{z}_1{}^{\mathrm{k}} + \mathbf{u}_1{}^{\mathrm{k}}\right\|_2^2 + \frac{\lambda}{2} \left\|\mathbf{x}^{k} - \mathbf{z}_2{}^{k} + \mathbf{u}_2{}^{k}\right\|_2^2, \tag{18}$$

which can be solved by finding the gradient,

$$\mathbf{x}^{k+1} = \left(\mathbf{\Psi}^{\mathrm{T}}\mathbf{\Psi} + \lambda\alpha_1 + \lambda\alpha_2\right)^{-1} \left\{\mathbf{\Psi}^{\mathrm{T}}\mathbf{s} + \lambda\alpha_1 \left(\mathbf{z}_1{}^{k} - \mathbf{u}_1{}^{k}\right) + \lambda\alpha_2 \left(\mathbf{z}_2{}^{k} - \mathbf{u}_2{}^{k}\right)\right\}. \tag{19}$$

Step 2: The problem of optimizing $\mathbf{z}_1$ and $\mathbf{z}_2$ can be solved by divide it into the following two sub-problems,

$$\mathbf{z}_1^{k+1} = \min_{\mathbf{z_2}} \left\|\mathbf{z}_1^{k+1}\right\|_1 + \frac{\lambda}{2} \left\|\alpha_2 \mathrm{CTV}\left(\mathbf{x}^{k+1}\right) - \mathbf{z}_1^{k} + \mathbf{u_1}^{k}\right\|_2^2, \tag{20}$$

$$\mathbf{z}_2^{k+1} = \min_{\mathbf{z_1}} \left\|\mathbf{z}_2^{k+1}\right\|_1 + \frac{\lambda}{2} \left\|\mathbf{x}^{k+1} - \mathbf{z}_2^{k} + \mathbf{u_2}^{k}\right\|_2^2. \tag{21}$$

The sub-problems can be solved by exploiting the iterative shrinkage threshold (ISTA),

$$\mathbf{z}_1{}^{k+1} = \mathrm{IST}\left(\mathrm{CTV}\left(\mathbf{x}^{k+1}\right) + \mathbf{u}_1{}^{k}, 1/\alpha_1\lambda\right), \tag{22}$$

$$\mathbf{z}_2{}^{k+1} = \mathrm{IST}\left(\mathbf{x}^{k+1} + \mathbf{u}_2{}^{k}, 1/\alpha_2\lambda\right), \tag{23}$$

where $\mathrm{IST}(x, \rho) = \mathrm{sign}(x) \cdot \max(|x| - \rho, 0)$ is the iterative shrinkage threshold function [45].

Step 3: Solving the Lagrange multipliers **u**

$$\mathbf{u}_i{}^{k+1} = \mathbf{u}_i{}^{k} + \mathbf{x}_i{}^{k+1} - \mathbf{z}_i^{k+1},\ i = 1, 2. \tag{24}$$

Algorithm 1 Sparse-TV algorithm

Input: The echo **S**, measurement matrix $\mathbf{\Psi}$, Parameters $\alpha_1, \alpha_2, \alpha_3$, and λ, maximum iterations K.
Output: The 3-D scattering coefficient $\mathbf{x}^K$

while not converge or $k < K$ **do**
  Update $\mathbf{x^{k+1}}$ by solving eq. (19).
  $\mathbf{z}_1{}^{k+1} = \mathrm{IST}\left(\mathrm{CTV}\left(\mathbf{x}^{k+1}\right) + \mathbf{u}_1{}^{k}, 1/\alpha_1\lambda\right)$
  $\mathbf{z}_2{}^{k+1} = \mathrm{IST}\left(\mathbf{x}^{k+1} + \mathbf{u}_2{}^{k}, 1/\alpha_2\lambda\right)$
  $\mathbf{u}_i{}^{k+1} = \mathbf{u}_i{}^{k} + \mathbf{x}_i{}^{k+1} - \mathbf{z}_i^{k+1}, i = 1, 2$
end while

RMA kernel based effective sparse-TV imaging

For solving the shortcoming that CS based algorithms relies heavily computing resource, the RMA kernel is proposed to replace the measurement matrix $\mathbf{\Psi}$. The RM kernel solve the iteration problem in the Fourier domain by exploiting the 2D fast Fourier transformation.

Consequently, we pad and transform the NLOS echo $\mathbf{S}_f \in \mathbb{C}^{\mathrm{N}_x \times N_z}$ from $\mathbf{S} \in \mathbb{C}^{\mathrm{MN}\times 1}$ by the function $F(\cdot){:}\mathbb{C}^{\mathrm{M}N\times 1} \rightarrow \mathbb{C}^{\mathrm{N}_x \times N_z}$ to perform the 2D Fourier transform of the corresponding size. And we suppose that $\mathbf{x}' \in \mathbb{C}^{\mathrm{N}_x \times N_z}$ is the matrix representing virtual imaging.

For the echo expressed in eq. (5), eq. (4) and its inverse operation can be written with RM kernel function as follow:

$$\mathbf{S}_f = \mathrm{RM}\{\mathbf{x}'\} = IFT_{2D}\{FT_{2D}\{\mathbf{x}'\} \odot \Phi_r\}, \tag{25}$$

$$\mathbf{x}' = \mathrm{RM}^{\dagger}\left\{\mathbf{S}_f\right\} = IFT_{2D}\left\{FT_{2D}\left\{\mathbf{S}_f\right\} \odot {\Phi_r}^{\dagger}\right\}, \tag{26}$$

where $\odot$ denotes the Hadamard product, $\mathrm{RM}(\cdot)$ and $\mathrm{RM}^{\dagger}(\cdot)$ are RM kernel and its inverse operation. Notably, eq. (25) is a classical near-field imaging assumption, and it suffers from decline when facing the downsampling performed.

The phase propagation matrix and its inverse which shown in eqs. (25) and (26) are defined as

$$\begin{aligned} \Phi_r &= {\mathbf{k}_y}^{-1}\mathrm{e}^{-\mathrm{j}\mathbf{k}_y r}, \\ {\Phi_r}^{\dagger} &= \mathbf{k}_y \mathrm{e}^{\mathrm{j}\mathbf{k}_y r}, \end{aligned} \tag{27}$$

where $\mathbf{k_y} \in \mathbb{C}^{\mathrm{N_x} \times \mathrm{N_z}}$ is described as the frequency wavenumber variable matrix.

We introduce the RM kernel and its inverse operation into the optimization problem described in eq. (15). The problem can be transformed into

$$\hat{\mathbf{x}} = \min_{\mathbf{x}} \alpha_1 \|\mathrm{CTV}(\mathbf{x})\|_1 + \alpha_2\|\mathbf{x}\|_1 + \frac{1}{2}\|\mathbf{S} - \mathrm{RM}\{\mathbf{x}\}\|_2^2 . \tag{28}$$

Since the RM kernel and its inverse kernel satisfy

$$\begin{aligned} \mathrm{RM}\left\{\mathrm{RM}^{\dagger}\{\mathbf{x}\}\right\} &= IFT_{2D}\left\{FT_{2D}\left\{\mathrm{RM}^{\dagger}\{\mathbf{x}\}\right\} \odot \Phi_r\right\} \\ &= IFT_{2D}\left\{FT_{2D}\left\{IFT\left\{FT\{\mathbf{x}\} \odot \Phi_r^{\dagger}\right\}\right\} \odot \Phi_r\right\}, \end{aligned} \tag{29}$$

the RM kernel based sparse-TV algorithm optimization is concluded as

$$\begin{cases} \mathbf{x}^{k+1} = \left(\mathbf{\Psi}^{\mathrm{T}}\mathbf{\Psi} + \lambda\alpha_1 + \lambda\alpha_2\right)^{-1}\left\{\mathbf{\Psi}^{\mathrm{T}}\mathbf{s} + \lambda\alpha_1\left({\mathbf{z}_1}^k - {\mathbf{u}_1}^k\right) + \lambda\alpha_2\left({\mathbf{z}_2}^k - {\mathbf{u}_2}^k\right)\right\}, \\ {\mathbf{z}_1}^{k+1} = \mathrm{IST}\left(\mathrm{CTV}\left(\mathbf{x}^{k+1}\right) + {\mathbf{u}_1}^k, 1/\alpha_1\lambda\right), \\ {\mathbf{z}_2}^{k+1} = \mathrm{IST}\left(\mathbf{x}^{k+1} + {\mathbf{u}_2}^k, 1/\alpha_2\lambda\right), \\ {\mathbf{u}_i}^{k+1} = {\mathbf{u}_i}^k + {\mathbf{x}_i}^{k+1} - \mathbf{z}_i^{k+1}, \ i = 1, 2. \end{cases} \tag{30}$$

Algorithm 2 RM-CSTV Algorithm

Input: The echo $\mathbf{S}$, measurement matrix $\mathbf{\Psi}$, Parameters α_1, α_2, and λ, maximum iterations K.

Output: The 3-D scattering coefficient $\mathbf{x}^K$

while not converge or $k < K$ **do**

Update $\mathbf{x}^{\mathbf{k+1}}$ by solving eq. (30).

${\mathbf{z}_1}^{k+1} = \mathrm{IST}\left(\mathbf{x}^{k+1} + {\mathbf{u}_1}^k, 1/\alpha_1\lambda\right)$

${\mathbf{z}_2}^{k+1} = \mathrm{IST}\left(\mathrm{CTV}\left(\mathbf{x}^{k+1}\right) + {\mathbf{u}_i}^k, 1/\alpha_2\lambda\right)$

${\mathbf{u}_i}^{k+1} = {\mathbf{u}_i}^k + {\mathbf{x}_i}^{k+1} - \mathbf{z}_i^{k+1}, i = 1, 2$

end while

NLOS region extraction and correction

In order to avoid the dependence on the prior information, a fast imaging of the *x*-*y* plane is first performed to perceive the horizontal wall shaped object in the NLOS scene. By Hough transform and NLOS geometric constraint which given in eq. (8), reflective surfaces in 2D slices are detected. Then, the NLOS imaging region is separated and corrected by eq. (7).

EXPERIMENTS AND RESULTS

In this section, the performance of proposed imaging method on NLOS 3-D sparse reconstruction is validated by NLOS high-resolution imaging experiment system, and the comparison of NLOS imaging by RM-CSTV, MSBP and mirror-symmetry based traditional compressed sensing (MSCS) method has been given, qualitative results are given with different sampling rates.

Considering the complexity of electromagnetic propagation in NLOS systems, it is difficult to simulate NLOS echoes accurately in a simulated system. Therefore, we use measured data to validate the imaging system and imaging algorithms.

To verify the imaging principle and algorithm performance of NLOS radar three-dimensional imaging. The imaging system consists of three parts: the data processing module, the radio frequency (RF) module, and the high-precision antenna motion rail module. The NLOS 3-D SAR imaging experimental system mainly uses the "TI AWR2243" millimeter-wave radar sensor and the "DCA1000" data acquisition card as the RF module, operating in a 1T1R single-input single-output (SISO) mode. The equivalent 2D virtual array is achieved using the antenna motion module.

For the antenna motion module, the synthesized array element has a length of 400 mm in both the *x*-axis and *z*-axis, i.e., $D_x = D_z = 400$ mm. To satisfy the condition of array without grating lobes, Array element spacing in the *x*-axis is set to $d_x = 1$ mm, and Array element spacing in the *z*-axis is set to $d_z = 2$ mm. The original data dimension size is $200 \times 400 \times 256$.

To validate the accuracy of the RM-CSTV algorithm for target localization and the quality of 3-D imaging, two sets of near-field NLOS imaging experiments were conducted using two metal tools and a metal flower stand as non-line-of-sight targets. Additionally, to achieve the experimental scene under ideal conditions, four pieces of the same mmW absorbing material were used to absorb possible clutter, and aluminum foil was pasted on the reflecting surface to achieve ideal reflection of electromagnetic waves on the reflecting surface.

To evaluate the performance of the proposed algorithm, this chapter mainly uses image entropy (ENT), image contrast (IC), image sharpness (SHA), and computation time for algorithm evaluation.

Image entropy is a statistical measure that reflects the average amount of information in an image. For the same imaging scene, a lower image entropy indicates a better focus effect and higher image quality, without causing any loss of image information. Image entropy can be defined as follows:

$$\mathrm{ENT} = -\sum_{i}\sum_{j}\sum_{k}|I_S(i,j,k)|^2 \log|I_S(i,j,k)|^2, \tag{31}$$

where $I_S(i,j,k)$ represents the complex value corresponding to the (i,j,k)th pixel in the 3-D imaging result.

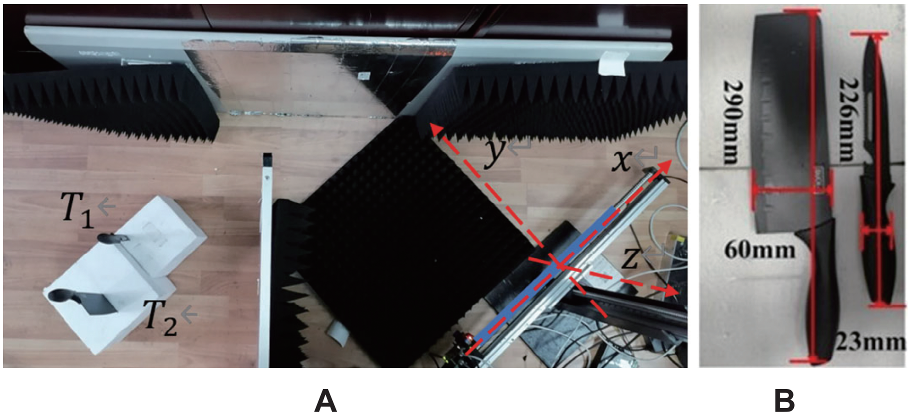

Figure 3 NLOS 3-D imaging experiment scene. (A) Metal knives experiment scenario; (B) optical images of metal knives.

Image contrast is an estimation of the distinguishable brightness levels, and higher contrast indicates better image quality. It can be represented as follows:

$$IC = \sqrt{\frac{I \times J \times K}{\|\mathbf{I}_S\|_2^2} \sum_i \sum_j \sum_k |I_S(i, j, k)|^4 - 1}, \tag{32}$$

where I, J, K denote the lengthes of 3-D result.

Image sharpness (SHA) is an indicator that reflects the clarity of the image plane and the sharpness of the image edges. The higher the image sharpness, the better the quality of test image.

$$\mathrm{SHA} = \sum_i \sum_j \sum_k |I_S(i, j, k)|^4. \tag{33}$$

The NLOS virtual target correction

As shown in Figure 3, the virtual antenna array is represented by the blue lines, which indicate the length and position of the array in the horizontal dimension. The gap width between the occluding surface and the reflecting wall is denoted by $d_w = 300$ mm, and the angle between the scanning array and the wall is denoted by $\theta_s = 50°$. The dimensions of the metal knives are shown in Figure 3B. The length and width of the kitchen knife are $L_1 = 290$ mm and $W_1 = 60$ mm, and the length and width of the small knife are $L_2 = 226$ mm and $W_2 = 23$ mm. The two knives are inserted into square foam blocks with side lengths of $L_3 = 200$ mm and $L_4 = 150$ mm.

Figure 4 represents the range-compressed echoes of the metal tools in the distance domain. The range echoes from the reflecting wall mainly concentrate around the 200th distance cell, while the echoes from the occluding surface are weaker due to the presence of absorbing material, and the targets echo is focused around the 100th distance cell. Around the 250th distance cell, clear pulse compression results provided by the two virtual knives can be observed, with the echo from target T_2 being significantly stronger than the target T_1 with a smaller reflecting cross section (RCS).

Significantly, the detection of NLOS target exists reflecting error. By exploiting mirror correction denoted at eq. (7), the maximum projection along the xz plane of NLOS 3-D result is shown in Figure 5. The sampling

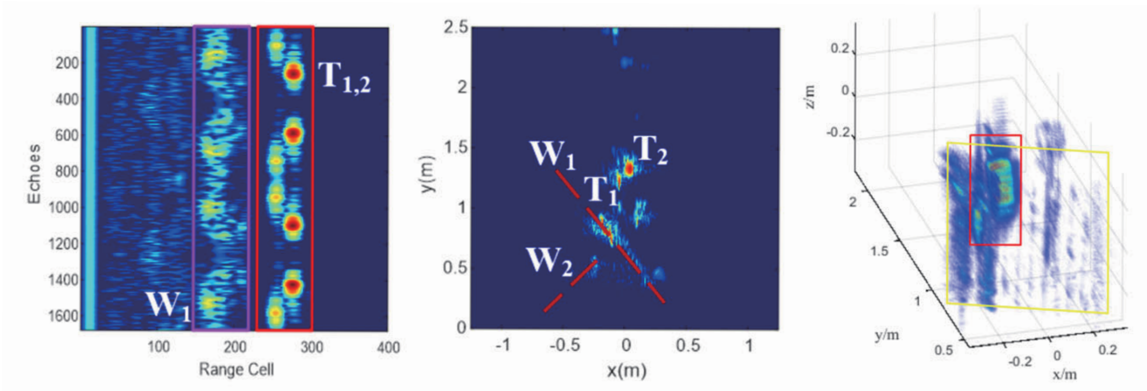

Figure 4 Echo data of knives. (A) Range-pulse compression result; (B) two-dimensional imaging results of the original NLOS echo; (C) three-dimensional imaging results of the original NLOS echo.

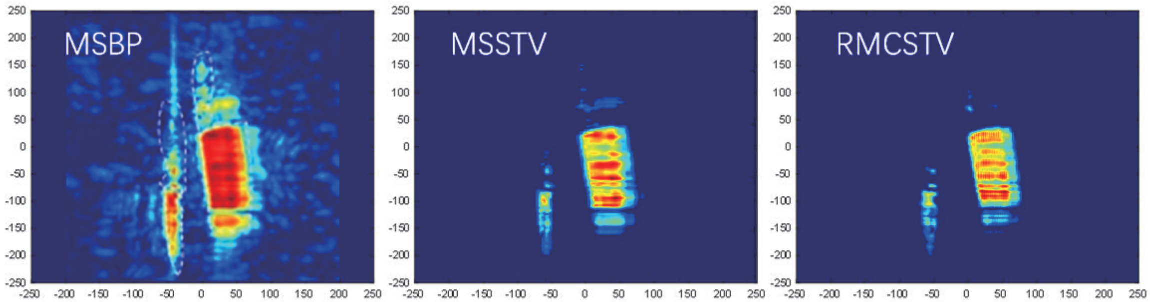

Figure 5 2D maximum projection results of NLOS 3-D imaging. (A) MSBP method; (B) MSCS method; (C) RM-CSTV method.

rate of the NLOS echo is 70%. BP, MSCS and RM-CSTV methods are exploited for 3-D reconstruction. As show in Figure 5C, the edge information is retained, and the reflecting error is corrected.

The 3-D imaging result

To verify the robustness of proposed method, ornaments are 3-D reconstructed as another NLOS targets. The experiment scene is built as shown in Figure 6. And the size of the ornaments are shown in Figure 6B.

For the NLOS experiments, we compare the performance of MSBP, RMA, CSTV, and RM-CSTV (Figures 7 and 8). As reported in Tables 1 and 2, CSTV method has the longest operation time because of relying on large-scale matrix operations and multiple iterations, which is far from meeting the real-time requirements in radar imaging, but it has high image contrast at each sampling rate. The RMA method has the lowest operation time, but its imaging quality is poor, and its imaging results deteriorate sharply as the sampling rate decreases. The various imaging metrics of the MSBP method are between the RMA method and the compressed sensing method.

Even in full sampling conditions, the BP and RMA imaging results are significantly affected by side lobes and clutter interference, with the edges of the objects being heavily polluted by noise. In contrast, the proposed algorithm effectively suppresses image side lobes and filters out a large amount of background

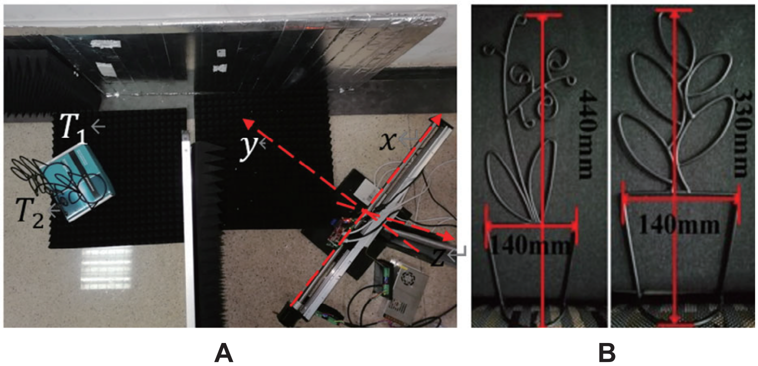

Figure 6 NLOS 3-D imaging experiment scene. (A) Metal knives experiment scenario; (B) optical images of metal knives.

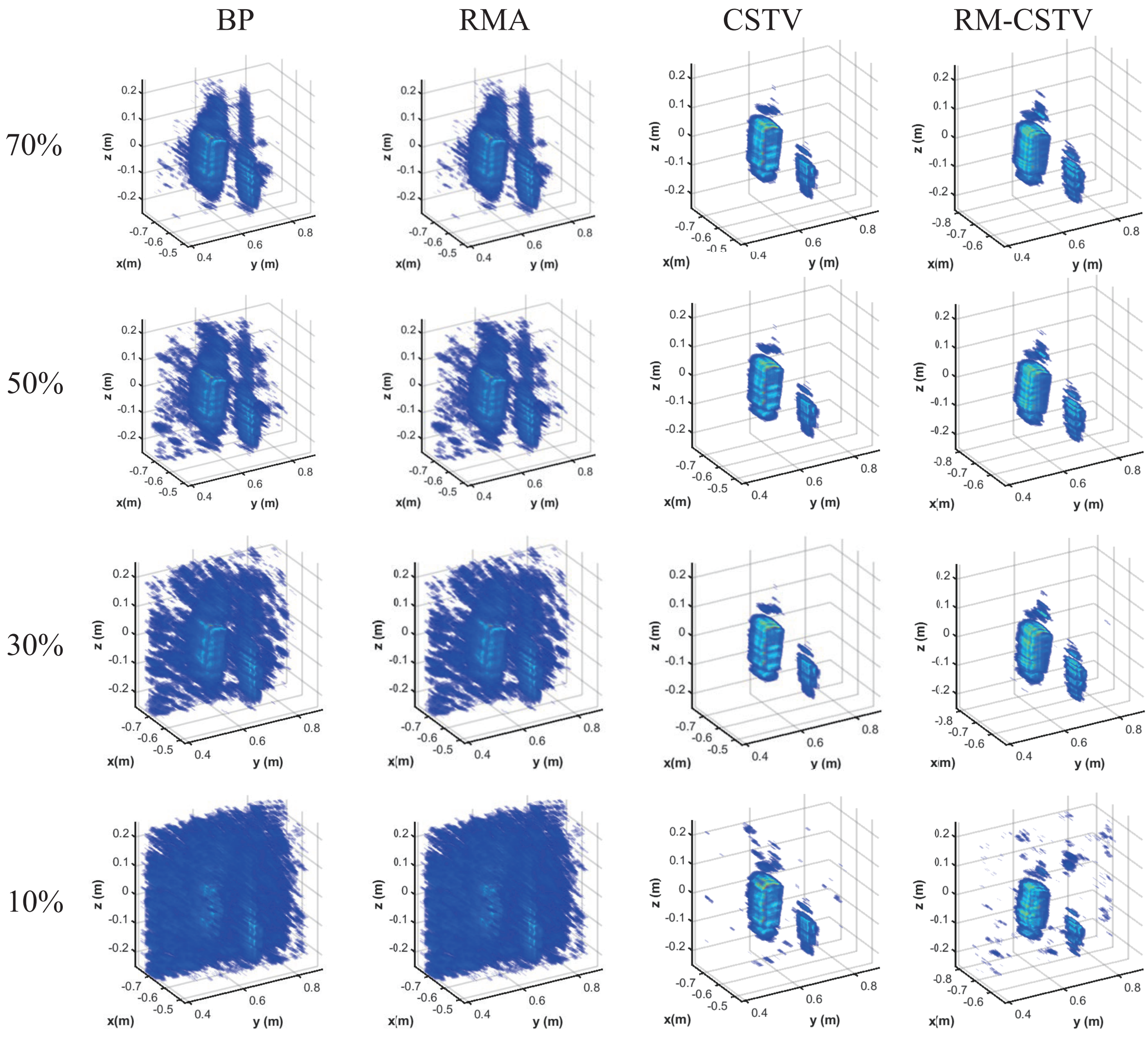

Figure 7 NLOS knives targets 3-D imaging result.

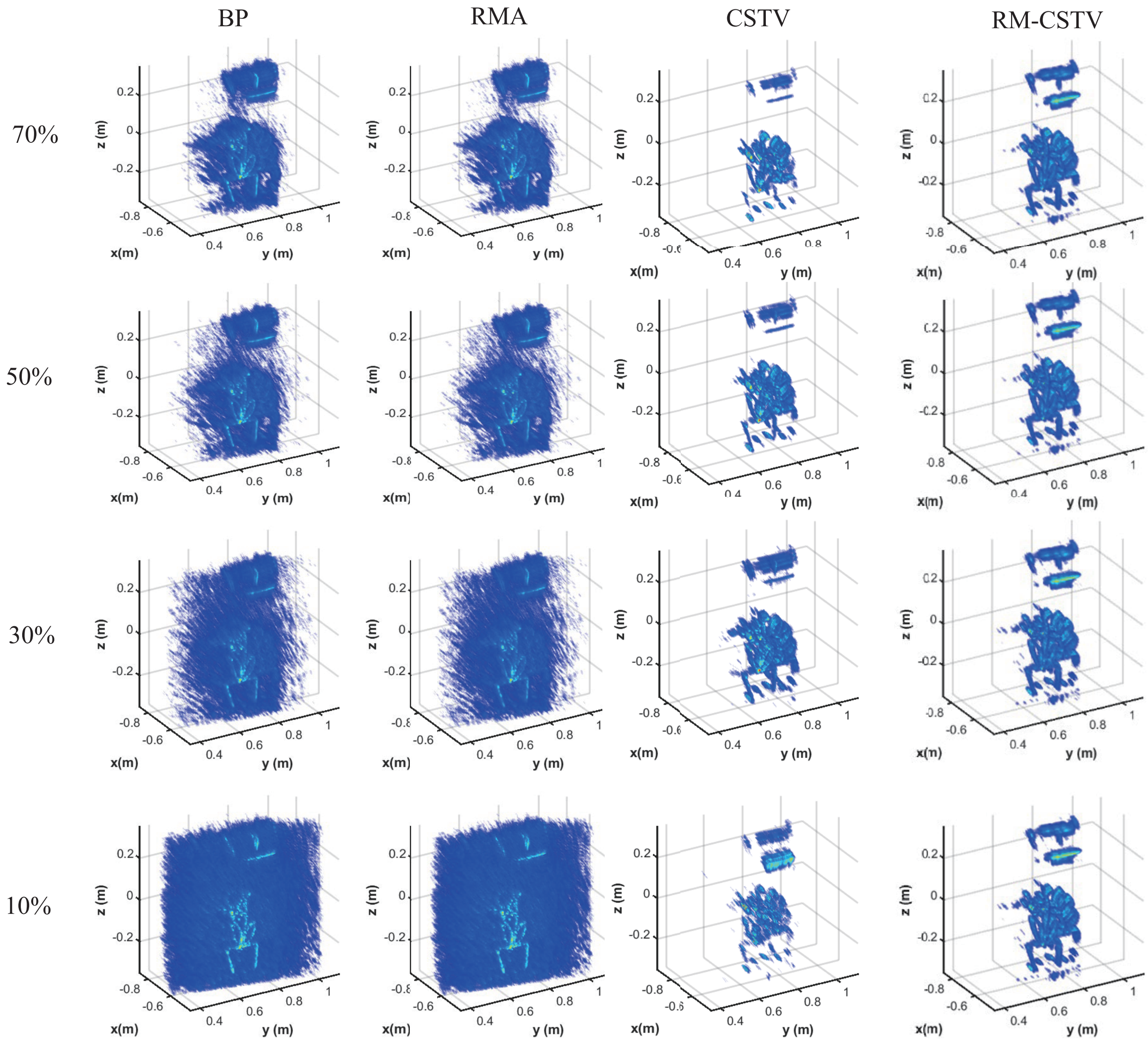

Figure 8 NLOS ornament targets 3-D imaging result.

clutter, resulting in clearer images and significantly improving imaging quality. Furthermore, the proposed algorithm successfully recovers partial detailed contours of the target even at low sampling rates, further proving the effectiveness and high performance of the algorithm.

Compared with the other three methods, the RM-CSTV method can achieve lower image entropy and higher image sharpness at the sampling rates of 70%, 50%, and 30%, which indicates that the proposed method has better image focusing effect. At the same time, the imaging time required by the proposed method is reduced by at least two orders of magnitude.

CONCLUSION AND DISCUSSION

In this article, we proposed an accelerated mmW NLOS 3-D sparse reconstruction method, i.e., RM-CSTV. The algorithm has the capability of not only reconstructing the NLOS targets with high resolution from multipath echoes in the LAC situation but also preserving the edge information. Using only a single radar

Table 1 Quantitative comparisons and speed evaluations of knives targets

Algorithm	Methods	Sampling rate (%)			
		70	50	30	10
BP	ENT	10.06	10.28	10.57	14.62
	IC	8.28	7.91	7.36	4.41
	SHA (dB)	70.95	70.69	70.4	69.98
	Time (s)	1420.29	913.51	589.64	293.73
RMA	ENT	10.50	11.06	12.01	18.52
	IC	9.72	8.08	7.54	3.77
	SHA (dB)	54.21	53.78	53.29	66.48
	Time (s)	54.21	53.78	53.29	4.72
CSTV	ENT	9.12	9.12	9.11	9.18
	IC	10.97	11.03	11.11	10.83
	SHA (dB)	67.7	68.21	65.84	66.14
	Time (s)	19024	15162	11029	7284
RM-CSTV	ENT	10.06	10.02	10.06	10.46
	IC	30.49	31.09	31.12	30.11
	SHA (dB)	75.3	75.31	75.15	67.52
	Time (s)	16.48	15.85	15.46	15.22

Table 2 Quantitative comparisons and speed evaluations of ornament targets

Algorithm	Methods	Sampling rate (%)			
		70	50	30	10
BP	ENT	13.41	13.63	13.98	14.62
	IC	7.87	7.37	6.48	4.41
	SHA (dB)	92.91	88.60	81.98	72.98
	Time (s)	1360.34	922.49	572.72	240.03
RMA	ENT	14.01	14.45	15.00	15.56
	IC	6.72	5.66	4.13	2.14
	SHA (dB)	154.57	147.07	127.06	102.17
	Time (s)	3.26	3.35	3.43	3.49
CSTV	ENT	11.08	11.57	12.11	12.35
	IC	22.46	17.29	12.89	12.22
	SHA (dB)	247.73	229.11	167.83	136.27
	Time (s)	18974	14312	10289	6850
RM-CSTV	ENT	11.82	11.85	11.97	13.68
	IC	14.55	14.43	13.88	8.17
	SHA (dB)	236.07	211.65	180.43	168.86
	Time (s)	15.02	14.22	14.16	14.68

array and single imaging, reflective surfaces are extracted from the LOS and NLOS mixed echoes and used to correct the position of the NLOS target. Considering the TV and sparse constraints of the target, the high-resolution problem of NLOS radar imaging is transformed into the optimization problem with multiconstraint. By solving the multiconstraint problem, defocuses of NLOS images are suppressed, and the contour information is preserved. Also, an RM kernel based accelerated algorithm is proposed to improve computational efficiency. With the RM-CSTV method, a well-focus and edge sharpness 3-D image can be obtained by the ADMM method to solve the optimization problem with sparse and TV constraints. Extensive NLOS 3-D mmW imaging experiments, including multitarget with 3-D characteristics, the weakly sparse surface target and weapons, validate the superiority of the RM-CSTV algorithm over the existing NLOS imaging methods in terms of both quality and efficiency. Except visually verifying that the NLOS imaging results of the proposed method have a precise contour, the indexes of ENT, Contrast, SHA and TBR are used to quantitatively ascertain the performance of our approach. Meanwhile, the acceleration method introduced RM kernel is two orders of magnitude times faster than the original method.

Funding

This work was supported by the National Natural Science Foundation of China (62271108).

Author contributions

X.L. and S.W. designed the research and analyzed the data. S.W. supervised the project. W.P., L.K. and X.Z. conducted the system demonstration and the experimental scheme designing. X.L. and X.C. collected the NLOS 3-D radar data. Y.W. and X.C preprocessed the data. Y.W. and S.G. analyzed the results. X.L. and S.W. co-wrote the manuscript. All authors contributed to the discussions.

Conflict of interest

The authors declare no conflict of interest.

References

1 Wu C, Liu J, Huang X, *et al*. Non-line-of-sight imaging over 1.43 km. *Proc Natl Acad Sci USA* 2021; **118**: e2024468118.
2 Faccio D, Velten A, Wetzstein G. Non-line-of-sight imaging. *Nat Rev Phys* 2020; **2**: 318–327.
3 Nam JH, Brandt E, Bauer S, *et al*. Low-latency time-of-flight non-line-of-sight imaging at 5 frames per second. *Nat Commun* 2021; **12**: 6526.
4 Wang Y, Zhang Y, Huang M, *et al*. Accurate but fragile passive non-line-of-sight recognition. *Commun Phys* 2021; **4**: 88.
5 Willomitzer F, Rangarajan PV, Li F, *et al*. Fast non-line-of-sight imaging with high-resolution and wide field of view using synthetic wavelength holography. *Nat Commun* 2021; **12**: 6647.
6 Kirmani A, Hutchison T, Davis J, *et al*. Looking around the corner using transient imaging. In: *Proceedings of the 2009 IEEE 12th International Conference on Computer Vision*. Kyoto: IEEE, 2009, 159–166.
7 Rapp J, Saunders C, Tachella J, *et al*. Seeing around corners with edge-resolved transient imaging. *Nat Commun* 2020; **11**: 5929.
8 Liu X, Wang J, Xiao L, *et al*. Non-line-of-sight imaging with arbitrary illumination and detection pattern. *Nat Commun* 2023; **14**: 3230.
9 Lindell DB, Wetzstein G, Koltun V. Acoustic non-line-of-sight imaging. In: *Proceedings of the IEEE/CVF Conference on Computer Vision and Pattern Recognition*. Long Beach: IEEE, 2019, 6780–6789.
10 Adib F, Katabi D. See through walls with WiFi! In: *Proceedings of the ACM SIGCOMM 2013 Conference on SIGCOMM*. Hong Kong, 2013, 75–86.
11 Chen S, Yang W, Xu Y, *et al*. AFall: Wi-Fi-based device-free fall detection system using spatial angle of arrival. *IEEE Trans Mobile Comput* 2023; **22**: 4471–4484.
12 Xiang Y, Guo S, Xia S, *et al*. NLOS target positioning method based on UAV millimeter-wave radar. *IEEE Sens J* 2024; **24**: 1975–1987.

13 Tang L, Guo S, Jian Q, *et al*. Through-wall human activity recognition with complex-valued range-time-doppler feature and region-vectorization convGRU. *IEEE Trans Geosci Remote Sens* 2023; **61**: 5111014.

14 Zhu Z, Guo S, Chen J, *et al*. Non-line-of-sight targets localization algorithm via joint estimation of DoD and DoA. *IEEE Trans Instrum Meas* 2023; **72**: 8506311.

15 Xue S, Guo S, Wu P, *et al*. NLOS target localization method in long L-shaped scenario with SISO UWB radar. In: *Proceedings of 2023 3rd International Conference on Frontiers of Electronics, Information and Computation Technologies (ICFEICT)*. Yangzhou: IEEE, 2023, 525–530.

16 Liu X, Chen J, Guo S, *et al*. Non-line-of-sight human vital sign detection method based on multipath signals fusion. In: *Proceedings of the 2023 3rd International Conference on Frontiers of Electronics, Information and Computation Technologies (ICFEICT)*. Yangzhou: IEEE, 2023, 489–496.

17 Shen Y, Zhang M, Wu Y, *et al*. Darting-out target detection with nlos signals for vehicle mimo mmwave radar. In: *Proceedings of 2023 IEEE Radar Conference (RadarConf23)*. San Antonio: IEEE, 2023, 1–6.

18 Wu P, Chen J, Guo S, *et al*. NLOS positioning for building layout and target based on association and hypothesis method. *IEEE Trans Geosci Remote Sens* 2023; **61**: 5101913.

19 Chen J, Guo S, Luo H, *et al*. Non-line-of-sight multi-target localization algorithm for driver-assistance radar system. *IEEE Trans Veh Technol* 2023; **72**: 5332–5337.

20 Li S, Guo S, Chen J, *et al*. Multiple targets localization behind L-shaped corner via UWB radar. *IEEE Trans Veh Technol* 2021; **70**: 3087–3100.

21 Shen R, Wei S, Zhou Z, *et al*. High resolution SAR tomography 3-D imaging via sparse recovery deep learning network. In: *Proceedings of 2022 3rd China International SAR Symposium (CISS)*. Shanghai: IEEE, 2022, 1–5.

22 Wang M, Wei S, Zhou Z, *et al*. 3-D SAR autofocusing with learned sparsity. *IEEE Trans Geosci Remote Sens* 2022; **60**: 5235818.

23 Zhou Z, Wei S, Zhang H, *et al*. SAF-3-DNet: Unsupervised AMP-inspired network for 3-D MMW SAR imaging and autofocusing. *IEEE Trans Geosci Remote Sens* 2022; **60**: 5234915.

24 Wei S, Zhou Z, Wang M, *et al*. Learning-based split unfolding framework for 3-D mmW radar sparse imaging. *IEEE Trans Geosci Remote Sens* 2022; **60**: 5229317.

25 Wang M, Wei S, Zhou Z, *et al*. 3-D SAR data-driven imaging via learned low-rank and sparse priors. *IEEE Trans Geosci Remote Sens* 2022; **60**: 5228117.

26 Lin Y, Qiu X, Li H, *et al*. Channel migration correction for low-altitude airborne SAR tomography based on keystone transform. *IEEE Geosci Remote Sens Lett* 2023; **20**: 4011805.

27 Lv X, Qiu X, Yu W, *et al*. Simulation-aided SAR target classification via dual-branch reconstruction and subdomain alignment. *IEEE Trans Geosci Remote Sens* 2023; **61**: 5214414.

28 Wang M, Wei S, Shi J, *et al*. 3-D SAR imaging via perceptual learning framework with adaptive sparse prior. *IEEE Trans Geosci Remote Sens* 2023; **61**: 5202716.

29 Ding C, Qiu X, Xu F, *et al*. Synthetic aperture radar three-dimensional imaging—From tomosar and array insar to microwave vision. *J Radars* 2019; **8**: 693–709.

30 Qiu X, Jiao Z, Peng L, *et al*. SARMV3D-1.0: Synthetic aperture radar microwave vision 3D imaging dataset. *J Radars* 2021; **10**: 485–498.

31 Qiu X, Jiao Z, Yang Z, *et al*. Key technology and preliminary progress of microwave vision 3D SAR experimental system. *J Radars* 2022; **11**: 1–19.

32 Du B, Qiu X, Zhang Z, *et al*. L_1 minimization with perturbation for off-grid tomographic SAR imaging. *J Radars* 2022; **11**: 62–70.

33 Wang M, Zhang Z, Qiu X, *et al*. ATASI-Net: An efficient sparse reconstruction network for tomographic SAR imaging with adaptive threshold. *IEEE Trans Geosci Remote Sens* 2023; **61**: 4701918.

34 Yang X, Fan S, Guo S, *et al*. NLOS target localization behind an L-shaped corner with an L-band UWB radar. *IEEE*

Access 2020; **8**: 31270–31286.

35 Guo S, Zhao Q, Cui G, *et al*. Behind corner targets location using small aperture millimeter wave radar in NLOS urban environment. *IEEE J Sel Top Appl Earth Observations Remote Sens* 2020; **13**: 460–470.

36 Chen J, Zhang Y, Guo S, *et al*. Joint estimation of NLOS building layout and targets via sparsity-driven approach. *IEEE Trans Geosci Remote Sens* 2022; **60**: 5114513.

37 Wen Y, Wei S, Liu X, *et al*. Non-line-of-sight isar imaging via millimeter-wave automotive radar. In: *Proceedings of the IGARSS 2023 - 2023 IEEE International Geoscience and Remote Sensing Symposium*. Pasadena: IEEE, 2023, 1229–1232.

38 Liu X, Wei S, Wei J, *et al*. Non-line-of-sight millimeter-wave radar 3-D sparse reconstruct via msstv method. In: *Proceedings of 2022 IEEE 9th International Symposium on Microwave, Antenna, Propagation and EMC Technologies for Wireless Communications (MAPE)*. Chengdu: IEEE, 2022, 424–427.

39 Wen Y, Wei S, Wei J, *et al*. Non-line-of-sight imaging of hidden moving target using millimeter-wave inverse synthetic aperture radar. In: *Proceedings of the IGARSS 2022 - 2022 IEEE International Geoscience and Remote Sensing Symposium*. Kuala Lumpur: IEEE, 2022, 555–558.

40 Wei J, Wei S, Zeng X, *et al*. Non-line-of-sight SAR imaging by multi-scattering of millimeter-wave. In: *Proceedings of the 2021 CIE International Conference on Radar (Radar)*. Haikou: IEEE, 2021, 259–263.

41 Cai X, Wei S, Liu X, *et al*. Compressed sensing imaging of mmw automotive radar via non-line-of-sight observation. In: *Proceedings of IGARSS 2023 - 2023 IEEE International Geoscience and Remote Sensing Symposium*. Pasadena: IEEE, 2023, 1225–1228.

42 Wei S, Wei J, Liu X, *et al*. Nonline-of-sight 3-D imaging using millimeter-wave radar. *IEEE Trans Geosci Remote Sens* 2022; **60**: 5106518.

43 Wei SJ, Zhang XL, Shi J. Compressed sensing linear array SAR 3-D imaging via sparse locations prediction. In: *Proceedings of 2014 IEEE Geoscience and Remote Sensing Symposium*. Quebec City: IEEE, 2014, 1887–1890.

44 Boyd S, Parikh N, Chu E, *et al*. Distributed optimization and statistical learning via the alternating direction method of multipliers. Found Trend Mach Learn, 2011; **3**: 1–122.

45 Bioucas-Dias JM, Figueiredo MAT. A new twist: Two-step iterative shrinkage/thresholding algorithms for image restoration. *IEEE Trans Image Process* 2007; **16**: 2992–3004.